

Unraveling the Water Degradation Mechanism of $\text{CH}_3\text{NH}_3\text{PbI}_3$

Chao Zheng* and Oleg Rubel*

Department of Materials Science and Engineering, McMaster University, Hamilton

E-mail: zhengc8@mcmaster.ca; rubelo@mcmaster.ca

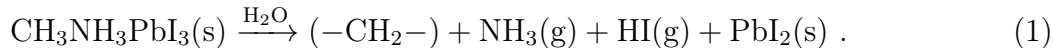
Abstract

Instability of perovskite photovoltaics is still a topic which is currently under intense debate, especially the role of water environment. Unraveling the mechanism of this instability is urgent to enable practical application of perovskite solar cells. Here, *ab initio* metadynamics is employed to investigate the initial phase of a dissolution process of $\text{CH}_3\text{NH}_3\text{PbI}_3$ (MAPbI₃) in explicit water. It is found that the initial dissolution of MAPbI₃ is a complex multi-step process triggered by the departure of Γ^- ion from the $\text{CH}_3\text{NH}_3\text{I}$ -terminated surface. Reconstruction of the free energy landscape indicates a low energy barrier for water dissolution of MAPbI₃. In addition, we propose a two-step thermodynamic cycle for MAPbI₃ dissolution in water at a finite concentration that renders a spontaneity of the dissolution process. The low energy barrier for the initial dissolution step and the spontaneous nature of MAPbI₃ dissolution in water explain why the water immediately destroys pristine MAPbI₃. The dissolution thermodynamics of all-inorganic CsPbI₃ perovskite is also analyzed for comparison. Hydration enthalpies and entropies of aqueous ions play an important role for the dissolution process. Our findings provide a comprehensive understanding to the current debate on water instability of MAPbI₃.

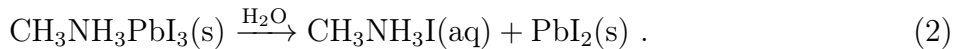
Introduction

Evolution of hybrid halide perovskite solar cells makes a contribution to the goal of replacement of fossil fuels. High power conversion efficiency and low fabrication cost raise perovskite photovoltaics as a tough competitor against the silicon solar cells. Since the inception of halide perovskite solar cells with 3.8% power conversion efficiency in 2009,¹ within 10 years of development, the world record power conversion efficiency of perovskite photovoltaics has reached 24.2% according to the efficiency chart published by the National Renewable Energy Laboratory. However, the poor stability of perovskite photovoltaic absorbers still remains unsolved and hinders the solar cells entering people's daily life.

Among the stimuli caused degradation of hybrid perovskite, water is confirmed to degrade MAPbI₃.² Whereas, the role of water incorporation into MAPbI₃ remains a topic of debate, with conflicting results reported in the literature. It is found the moisture invasion fractures the connection of C–N in CH₃NH₃ (MA) and generate ammonia and hydrogen iodide^{3,4}



Kakekhani et al.⁵ propose a super-hydrous state of water incorporation in MAPbI₃ to explain deterioration of its photovoltaic properties in a moist environment. Besides, Philippe et al.⁶ and Niu et al.⁷ proposed a decomposition mechanism relating to the presence of CH₃NH₃I (MAI) and PbI₂,



In fact, two extreme water content conditions are discussed above: atmospheric moisture and liquid water. Both of the mechanisms are important. For fresh perovskite photovoltaics, moisture degradation is obviously important for the endurance. There are plenty of publications investigating the moisture induced degradation of CH₃NH₃PbI₃.^{8–15} As photovoltaics, it has to be considered that different situations the cells will encounter, e.g. after couple of years, cracks of the photovoltaic modules are inevitable.¹⁶ At this stage, understanding of liquid water degradation mechanism becomes important. Especially, hybrid halide perovskites contain lead element. There are less investigations about the liquid water degradation pathway.^{17–19} It is still unclear about the mechanism of CH₃NH₃PbI₃ degradation in liquid water, such as the energy barrier, decomposition details.

Key challenges in understanding the degradation mechanism of MAPbI₃ are the difficulties in determining the surface chemistry of the first few atomic layers of the pristine material without any exposure to ambient atmospheric conditions, and, conversely, the difficulties in measuring this same surface chemistry in real time under exposure to realistic environments.⁴ Molecular dynamics (MD) make it possible to explore the degradation mech-

anism at the atomic level. Mosconi et al.¹⁷, Caddeo et al.¹⁹ simulated the heterogeneous interface between water and MAPbI₃ to study its water degradation mechanism. Mosconi et al.¹⁷ observed first MAI unit dissolved within 8.5 ps using an *ab initio* molecular dynamics (AIMD). Caddeo et al.¹⁹ observed a fast dissolution of outermost MAI-terminated layers within 10 ps using classical molecular dynamics. Whereas, the details of the initial phase of the degradation process, such as energy barriers of corresponding steps, and the preference of ions leaving the surface are still missing. We performed AIMD simulation for water and MAPbI₃ interface aiming to clarify the degradation mechanism of MAPbI₃ in water. Contrary to previous reports of a short degradation time, our AIMD simulation of the heterogeneous interface renders no dissolution event happening within 12 ps. This phenomenon questions the immediacy of MAPbI₃ degradation in water.² During 12 ps standard AIMD simulation, we observed both I⁻ and MA⁺ ions trying to detach from the MAPbI₃ surface. As time passed by, the ions retrace back to the Pb-I framework cavity. Thus, the dissolution event reported in Ref. 17 could be an artefact due to a limited simulation time of about 10 ps.

The ionic nature of MAPbI₃^{8,20} allows to draw a parallel to the research on simulation of NaCl dissolution. Intriguingly, Liu et al.²¹ and Chen et al.²² encountered the same situation when dissolving NaCl using MD. A single ionic dissolution is a rare event, which is unlikely to happen on the time scale of an AIMD simulation. Therefore, the dissolution needs to be "driven" artificially.²² Metadynamics²³⁻²⁵ is a powerful algorithm that can be used both for probing the free energy landscape and for accelerating rare events in systems described by complex Hamiltonians, at the classical or at the quantum level. Since the dissolution of MAPbI₃ in water is viewed as a rare event, it needs a much longer simulation time to capture the dissolution, and this finding raises a question about validity of conclusions drawn from the relatively short 10 ps simulation.¹⁹

In the current research, we propose the water degradation mechanism employing the capability of *ab initio* metadynamics which uses computational sands to fill the initial po-

tential valley and to force the trapped system from the initial basin and explore the energy landscape. And it gives the possibility to describe the heterogeneous interface with a large system from the atomic level, dynamically and considering finite temperature effects. Hence, the method can accelerate and capture the dissolution process of MAPbI₃ in water. Here, the free energy surface (FES) of water dissolution MAPbI₃ can be reconstructed based on the historical computational sands added to the basin. The obtained FES suggests a relatively low energy barrier of the first step of the dissolution process. In addition, an analysis based on a thermodynamic cycle for dissolution MAPbI₃ explains the intrinsic water instability of MAPbI₃. The low dissolution energy barrier and spontaneous dissolving trend together unravel the fragile nature of MAPbI₃ when encountering water.

Computational method

Electronic structure calculations have been performed in the framework of DFT²⁶ and Perdew-Burke-Ernzerhof generalized gradient approximation²⁷ (GGA-PBE) for the exchange-correlation functional. Van der Waals correction is important for halide hybrid perovskite.^{28,29} Among different van der Waals corrections, Li and Yang³⁰ employed both optb86B-vdW³¹ and PBE+D3 method³² to optimize structures. The results show that both the vdW functionals can give accurate crystal structure predictions. And the PBE+D3 method acts even better than optb86B-vdW when comparing with experimental data. Except for the structural properties, our previous work²⁹ analyzed the polymorphism of MAPbI₃ employing different functionals including PBE+D3. We concluded that the PBE+D3 can accurately predict the trend of polymorphism of MAPbI₃. It indicates PBE+D3 can capture the total energy estimation very well. Hence, the PBE+D3 level van der Waals correction is considered for all calculations. Total energies of all compounds were obtained using the Vienna *ab initio* simulation program (VASP) and projector augmented-wave (PAW) potentials.³³⁻³⁵

The phase separation energy difference ΔE_{tot} of MAPbI₃ and CsPbI₃ are adopted from our previous calculations.³⁶ For reciprocal space integration, $3 \times 3 \times 2$ Monkhorst-Pack grid³⁷

was used for tetragonal MAPbI₃, 4 × 4 × 3 for hexagonal PbI₂ and 3 × 6 × 2 for orthorhombic CsPbI₃. The convergence of ΔE_{tot} with respect to the k-mesh density was tested via doubling the density for investigated perovskite structures and corresponding decomposed structures. And the convergence is better than 5 meV. The cutoff energy for a plane wave expansion was set at 400 eV. The lattice constant and atomic positions were optimized such that residual forces acting on atoms did not exceed 2 meV/Å, and the residual hydrostatic pressure was less than 50 MPa.

For AIMD calculations, a semi-empirical scaling method^{38,39} is used to achieve a finite-temperature structure of MAPbI₃ that is self-consistent with PBE functional with the van der Waals correction. According to scanning tunnelling electron microscopy studies of MAPbI₃,^{40,41} we selected a MAI-terminated (001) surface structure of tetragonal MAPbI₃. The MAPbI₃ slab was modelled as 2 × 2 in plane per-optimized tetragonal supercell with the thickness of 7 atomic layers spaced by 18.6 Å filled by water molecules (see Fig. 1). The number of water molecules embedded is 158 which is obtained based on the experimental liquid water density. The dimension of the periodic cell are $a = b = 17.72$ Å which corresponds twice of the size of tetragonal MAPbI₃. In total, we have $c = 38.35$ Å for the heterogeneous structure. In order to obtain an initial randomization of the atomic positions, we performed a standard AIMD simulation in two stages: pre-heating followed by a fixed temperature relaxation. Pre-heating from 0 to 300 K was performed in 700 steps (step size of 1 fs) using a linear ramp-up function (VASP tag SMASS = -1). Velocities were scaled every 20 MD steps. Although the orientations of MA⁺ cations on surface are anisotropic after this two-stage relaxation, we noticed the -NH₃⁺ groups of MA⁺ ions are attracted by oxygen atoms from adjacent water molecules during relaxation. Accuracy of computed Hellmann-Feynman forces was determined by the energy convergence criterion of 10⁻⁶ eV. Only one k point at Γ was used to sample the Brillouin zone. Atomic positions and velocities at the end of the preheating stage were taken as the input for the fixed temperature relaxation. The fixed temperature relaxation was conducted at 300 K for ~ 9.8 ps (step size

of 1 fs). A Nosé–Hoover thermostat^{42,43} was used to stabilize the temperature (VASP tag SMASS = 0). Atomic positions during AIMD were stored every 20 steps. Crystallographic information files (CIF) with atomic structures used in calculations can be accessed through the Cambridge crystallographic data centre (CCDC deposition numbers 1919295–1919299).

Metadynamics was applied to accelerates the rare events of the heterogeneous interface (VASP tag MDALGO = 21). It is realized by augmenting the system Hamiltonian $\tilde{H}(t)$ with a time-dependent bias potential $\tilde{V}(t, \xi)$ which acts on selected collective variables $\xi = \{\xi_1, \xi_2, \dots, \xi_m\}$

$$\tilde{H}(t) = H + \tilde{V}(t, \xi) , \quad (3)$$

where H stands for the original Hamiltonian of unbiased system. $\tilde{V}(t, \xi)$ is defined as a sum of Gaussian hills with height h and width w ,

$$\tilde{V}(t, \xi) = h \sum_{i=1}^{\lfloor t/t_G \rfloor} \exp \left[-\frac{|\xi(t) - \xi^{(i \cdot t_G)}|^2}{2w^2} \right] . \quad (4)$$

During the metadynamic simulation, $\tilde{V}(t, \xi)$ is updated by adding a new Gaussian with a time increment t_G which is set to 100 fs. A collective variable (CV) is a function of the particle positions. We employed two CVs in the current metadynamics. The first CV (ξ_1) is defined as the coordination number

$$\xi_1 = \sum_{i=1}^M \frac{1 - (q_i/c_i)^9}{1 - (q_i/c_i)^{14}} \quad (5)$$

of the departing Γ^- (or N atom of monitored MA^+ during a paralleled MA^+ dissolution) with the rest Γ^- (or N atoms of other MA^+) in the topmost complete layer of the surface. M is the number of Γ^- in the topmost layer except the monitored Γ^- (or N atom in MA^+). c_i is defined as the interatomic distance between the monitored Γ^- (or N atom in MA^+) and each rest of Γ^- (or N atom in MA^+) in the initial state. q_i is the on-the-fly interatomic distance between the monitored Γ^- (or N atom in MA^+) and each rest of Γ^- (or N atom in MA^+) during the

simulation.

The second CV (ξ_2) records the interatomic distance between the monitored Γ^- and Pb^{2+} underneath it. An estimate of the underlying free energy $A(\xi)$ can be obtained via a sufficiently long time simulation,

$$A(\xi) = \lim_{t \rightarrow \infty} \tilde{V}(t, \xi) + \text{const} . \quad (6)$$

The choice of coordination numbers and Pb–I distance as two CVs is because these CVs vary according to different dissolution stages. CV (ξ_2) directly indicates the dissolution process of the monitored Γ^- ion. However, only CV (ξ_2) is not sufficient to tell the difference between the states of Γ^- ion attached on surface and further dissolution in water. CV (ξ_1) is able to reflect the bond breaks accompanying the leaving of Γ^- ion. Combination with CV (ξ_1), it is clear to explore an intermediate state. Liu et al.²¹ used different combination of CVs and determined that the settings same as we used are the best combination to characterize the dissolution event.

After the standard ~ 9.8 ps MD, the width of Gaussian hill is determined from a continuous 1.8 ps metadynamics which monitors the two CVs without adding hills. The amplitudes of these CVs in the reactant well indicate the width of the well,⁴⁴ and we set $w = 0.11$. Considering our large system (more than 800 atoms) and complexity of the dissolution procedure, we set $h = 0.026$ eV from IS to IM. After passing the IM state, we increased the Gaussian height to 0.052 eV. To characterize the hydrogen bonds between water molecules and Γ^- , we set the bonding searching range to 3.25 Å.⁴⁵ `Plumed` package⁴⁶ and `Gnuplot` were utilized to reconstruct and plot the FES of dissolution events. `VESTA 3` package⁴⁷ was used to visualize crystal structures.

Results and discussion

Dissolution energy barrier estimation

In this section, it will be shown that MAPbI₃ dissolution is a complex multi-step process triggered by the initial departure of I⁻ ions from the MAI-terminated surface. The choice of the MAI-terminated surface as a starting point is based on the scanning tunnelling microscopy topography observations of halide hybrid perovskite surface.^{40,41} An intermediate state is identified as the departing ion is partially hydrated but still remains within a proximity from the MAPbI₃ surface. Starting with an equilibrated configuration we performed metadynamics using biasing variables (see Method section) aimed at obtaining the lowest free energy pathway for the detachment of I⁻ from the MAPbI₃ surface.

We begin with the discussion of dissolving I⁻ using the metadynamics. An equilibrated heterogeneous interface is taken as the initial structure for metadynamic simulation of the dissolution process. The observation of I⁻ or MA⁺ ion backtracking to Pb–I cavity in the previous discuss is due to the trapping of the system in the initial FES basin using standard AIMD. The configuration trapped at this basin is named as the initial state (IS) shown in Fig. 1. In the IS, the monitored I⁻ (labelled yellow) forms hydrogen bonds with two water molecules above it, and bonds with a lead atom underneath it. Under the action of the metadynamic bias, the system is discouraged to revisit previous explored spots. With accumulating the computational sands, the initial basin is filled and the system is forced to escape from the local minima. We observe the elongation of the I–Pb bond shown in Fig.2a and Fig.2b. After around 7 ps of metadynamic simulation, the system arrives at the first transition state (TS^I) of the dissolution process shown in Fig. 2c and Fig. 2d, the I–Pb bond breaks. At the transition state, the I⁻ ion retains two hydrogen bonds with two water molecules. Besides, the I⁻ forms bonds with a hydrogen atom on –NH₃⁺ group of one MA⁺, and with a hydrogen atom on –CH₃ group of the another MA⁺. The interatomic distance of the monitored I–Pb bond stretches from 3.22 Å at IS to 5.27 Å at TS^I. We

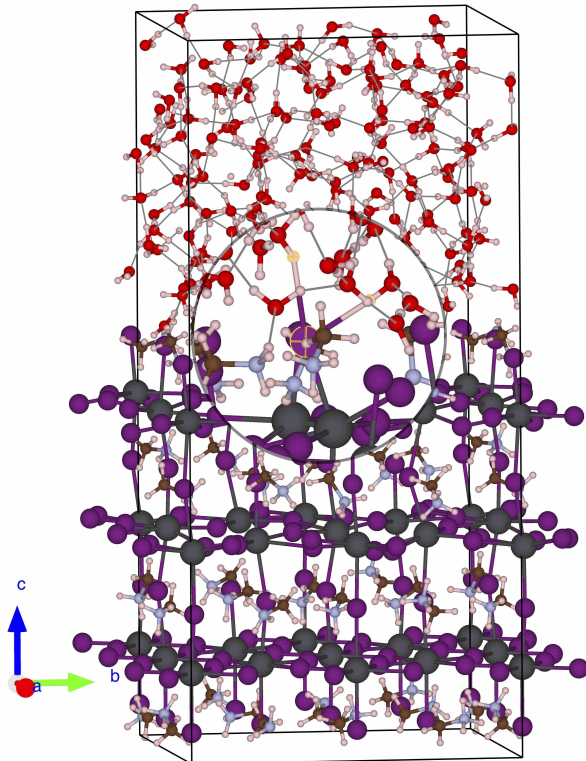


Figure 1: The initial state (IS) configuration of water/MAPbI₃ interface. Light pink represents hydrogen atoms. Red represents oxygen atoms. Brown represents carbon atoms. Light purple represents nitrogen atoms. Grey represents lead atoms. Purple represents iodine atoms.

continued the metadynamic simulation after conquering the TS^I. The lifted I⁻ drifts away from the underneath Pb²⁺. Meanwhile, neighbour MA⁺ cations of the monitored I⁻ drift towards the cavity. It is intriguing to find that the departing I⁻ ion does not enter solvent immediately and the surrounding MA⁺ cations do not leave the lattice following the I⁻ ion. The heterogeneous interface evolves towards a state in which the I⁻ is partly hydrated, but remains trapped close to the surface illustrated in Fig. 2e and Fig. 2f. We assign this local energy minimum as an intermediate state (IM). The partially hydrated I⁻ is in an adatom-like configuration. Upon transition from TS^I to IM, the coordination number of the I⁻ with the solvent water molecules increases from ~ 2 to ~ 4 .

During the whole simulation, we find the system spends a long time at IM basin. The partly hydrated I⁻ stays on top of one neighbour MA⁺ cation due to an electrostatic attrac-

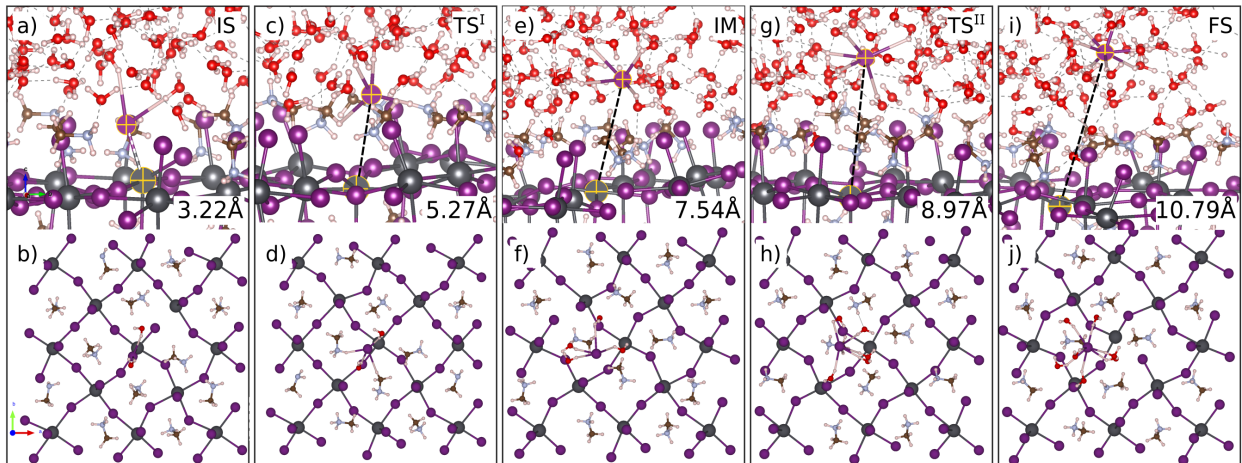


Figure 2: The initial state (IS), first transition state (TS^I), intermediate state (IM), second transition state (TS^{II}) and final state (FS) of the initial dissolution of $MAPbI_3$ in water, respectively. I–Pb interaction is marked as dashed line, and the value is shown in each configuration. It is clear to see that the I–Pb bond breaks at TS^I and the monitored I^- detaches surface at TS^{II} . Lower panel shows the corresponding topview of each configuration.

tion. Once the IM basin is filled, the system comes to the second transition state (TS^{II}), the corresponding configuration is shown in Fig. 2g and Fig. 2h. From IM to TS^{II} , the pulls from water molecules acting on the I^- gradually overwhelm the interactions between the I^- and underneath MA^+ . The adatom-like I^- ion detaches from the MA^+ cation. The number of water molecules in the hydration shell of I^- increase to 5. The system needs to conquer the barrier of 0.22 eV to reach TS^{II} . This relatively larger energy barrier (compared with the initial 0.16 eV) is explained by breaking of the electrostatic attraction between the leaving I^- and MA^+ . After passing through the TS^{II} , the system evolves to a final state (FS) shown in Fig. 2i and Fig. 2j. We characterize the FS as a state where I^- escapes from the $MAPbI_3$ surface and fully dissolves in water. In the FS, I^- ion is coordinated by ~ 7 water molecules, consistent with both experimental and *ab initio* simulated coordination number of 6–9.^{45,48} The overall energy barrier for the initial dissolution event is obtained as the energy difference between the IS and TS^{II} which is 0.18 eV.

We portray the FES of the dissolution process of $MAPbI_3$ in water in Fig. 3. The ease of

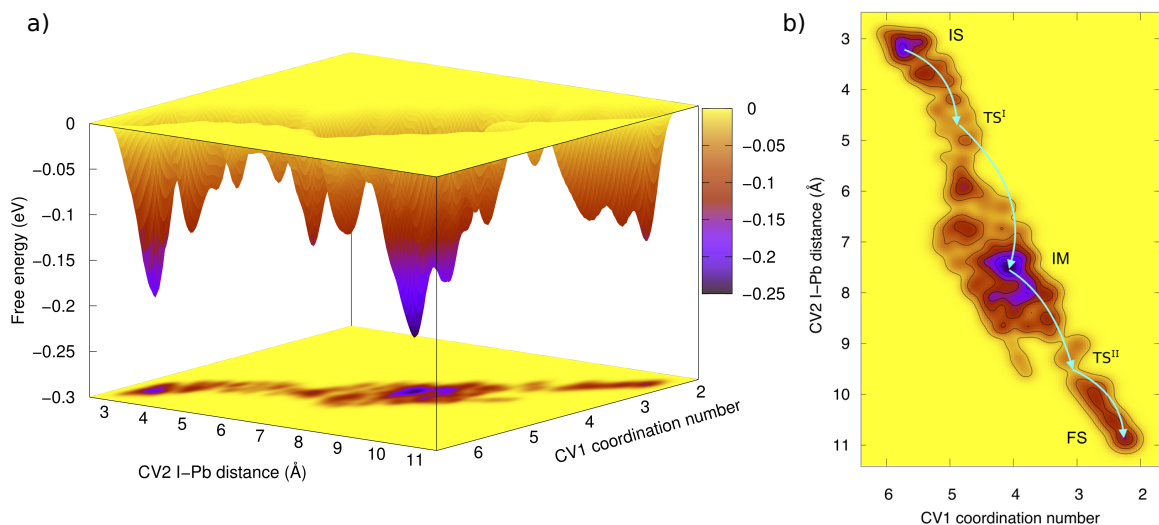


Figure 3: Reconstructed free energy surface of dissolution of MAPbI_3 in water from metadynamic simulation. a) gives the free energy landscape of the dissolution process of MAPbI_3 in water. b) is the contour plot of the free energy surface. Arrows point steps on the dissolution pathway.

the first dissolution event happening is determined by an energy barrier between IS and TS^{I} . Figure 3 suggests that the initial configuration needs to conquer 0.16 eV energy barrier to break the I–Pb bond in aqueous environment to reach TS^{I} . For comparison, Caddeo et al.¹⁹ reported an energy barrier of 0.36 eV consisting of a layer-by-layer degradation of MAPbI_3 in water. Lin et al.⁴⁹ reported a larger energy barrier (greater than 0.5 eV) when dissolving an Γ^- from CsPbI_3 surface in water. Releasing the Γ^- is a competition between the hydration by water molecules and the electrostatic attraction to atoms on the surface and in the bulk of MAPbI_3 . From a thermodynamic point of view, the dissolution phenomenon is an effect of compensating electrostatic energy stored in the MAPbI_3 surface by heat released from the hydration of the Γ^- . This process is further promoted by the entropy gain during Γ^- entering

water. Detailed thermodynamic analysis of the overall dissolution process is discussed in the following section. Both the hydrophilicity of Γ^- and MA^+ ion and the intrinsic low electrostatic energy of MAPbI_3 ^{8,36} contribute to these very low energy barriers in Fig. 3.

Simulations of NaCl dissolution in water identify a clear preference for the dissolution of Cl^- as the initial step over Na^+ .^{21,50,51} To investigate the preference of ions leaving MAPbI_3 surface at the beginning of the dissolution process, we performed an alternative metadynamic simulation where the dissolution starts with MA^+ . The FES of dissolution of MA^+ is constructed and it renders a deeper energy basin (~ 0.31 eV), shown in Fig. S1. However, we only obtained the FES for the initial basin of the dissolution of MA^+ . We find that the initial basin of MA^+ dissolution is much wider and deeper than the case of Γ^- ion. Although we use relative large Gaussian height and weight, it is hard to explore the sequent stages of MA^+ dissolution in water. A larger Gaussian will accelerate the exploration, however, sacrifice of accuracy is expected. Due to the capability of our facility and limited time, we stopped here for exploring the sequent FES of MA^+ dissolution in water. The shape and rotational property of MA^+ ion may contribute to the large initial basin.

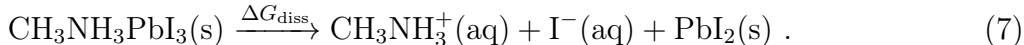
The difference of the initial basins indicates Γ^- is relatively easier to dissolve in water. Although $-\text{NH}_3^+$ group of MA^+ is hydrophilic, the connected $-\text{CH}_3$ group is hydrophobic. When dissolving MA^+ in water, the hydrophobic $-\text{CH}_3$ group needs more space to settle in water molecules.⁵² Seeking for more space in water molecule network and breaking the interactions of MA^+ with surrounding ions in MAPbI_3 surface together lead to a higher energy barrier for the first dissolution of MA^+ . As a result, the lower energy barrier suggests a priority of Γ^- leaving the surface. Note that in the supporting information of Caddeo et al.¹⁹, their simulation indicates that the first step of the dissolution MAI-terminated surface in water is releasing MA^+ at 5 ps. Differently, during our over 33.5 ps simulation time including equilibrium relaxation and metadynamics, we only observe the dissolution of one Γ^- ion in water. Liu et al.²¹ indicated a forcefield-based description of NaCl dissolution in water failed to capture a preference for Cl^- over Na^+ dissolution. Limitations related to a

proper description of bond breaking or formation in the empirical potential framework may contribute to this discrepancy.

It is worthy to note that we didn't observe any decomposition of MA^+ cation during the whole simulation. Compared with the high deprotonation energy (~ 4.03 eV) of MA^+ cation,⁵³ the low energy barrier of releasing I^- suggests the initial degradation MAPbI_3 in water is the dissolution of MAI-terminated layer into water solute. It is meaningful to mention that the energy barrier of transformation of the PbI_2 2D-planer layer to PbI_2 trigonal configuration is around 0.26 eV.⁵⁴ Considering the low energy barriers of dissolving I^- in water as well the low energy barriers of decomposition of Pb-I layer, the overall degradation energy barrier of MAPbI_3 dissolution in water is less than 0.3 eV.

Thermodynamics of MAPbI_3 dissolution in water

Followed by the discussion of the initial process of MAPbI_3 dissolution in water, the thermodynamic analysis of the overall decomposition is proceeded in this section. It is also intriguing to investigate how CsPbI_3 reacts with water as a comparison. The dissolution of MAPbI_3 via water can be described as follow:



Estimation of the change of the Gibbs free energy (ΔG_T°) between the reactants and products is a standard approach for predicting whether a reaction or process will occur spontaneously. Combination of the density functional theory (DFT) calculation with additional thermodynamic data (see Chap. 7 in Ref. 55) is used to predict ΔG_T° of phase separation of MAPbI_3 .⁵⁶ Kye et al.⁵⁷ utilize an *ab initio* thermodynamic formalism with the effect of solution to investigate the behaviour of defects on phase stability of CsPbI_3 . Here, we apply the combination of theoretical and experimental data to estimate the Gibbs free energy change (ΔG_{diss}) of MAPbI_3 dissolution in water at temperature T as stated in Eq. (7). According

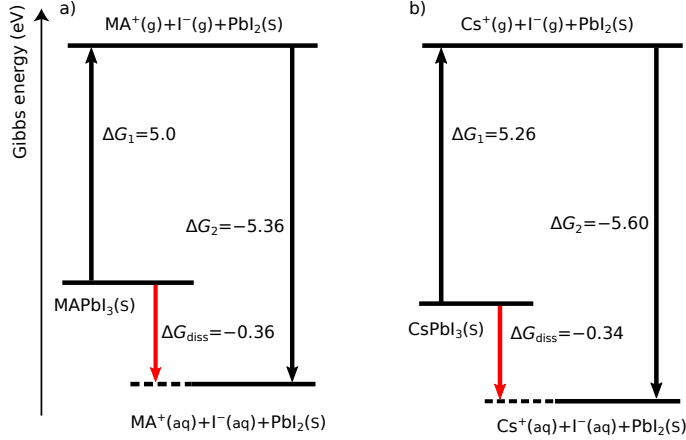


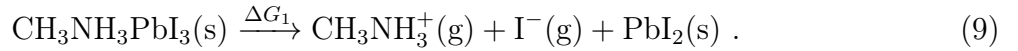
Figure 4: A thermodynamic cycle for the calculation of the dissolution Gibbs free energy change (ΔG_{diss}) for (a) MAPbI₃ and (b) CsPbI₃ in water.

to Sholl and Steckel⁵⁵, G_T° can be expressed as,

$$G_T^\circ = E_{\text{tot}} + \tilde{\mu}_T^\circ . \quad (8)$$

Here, E_{tot} is the standard state enthalpy at zero temperature which is evaluated based on DFT total energy calculations. $\tilde{\mu}_T^\circ$ captures finite temperature effects on the chemical potentials of species involved which is evaluated from NIST-JANAF thermochemical tables as well as other experimental resources.

In order to capture ΔG_{diss} at finite temperature, we designed a two-step thermodynamic cycle as shown in Fig. 4a. The first step of the thermodynamic cycle is the dissociation of MAPbI₃(s) to oppositely charged ions MA⁺(g) and I⁻(g) and PbI₂(s),



During this process, finite temperature effect on enthalpies and entropies of the system from solid initial state to intermediate gaseous state and PbI₂(s) are evaluated, respectively

$$\tilde{\mu}_T^\circ = H_T^\circ - H_{0\text{K}}^\circ - TS_T^\circ . \quad (10)$$

The addition of the resultant $\tilde{\mu}_T^\circ$ and calculated E_{tot} generates G_T° of each species. Related thermodynamic properties of species involved in the first step of the thermodynamic cycle of MAPbI₃ dissolution in water are listed in Table 1. According to Table 1, it is feasible to

Table 1: Electronic total energy E_{tot} per formula unit (f.u.), $H_T - H_{0\text{K}}$, standard state entropy S_T° , the chemical potential $\tilde{\mu}_T^\circ$ and standard Gibbs free energy G_T° in the first step of the thermodynamic cycle involving MAPbI₃ dissolution in water. Here, we focus on room temperature $T = 298.15$ K.

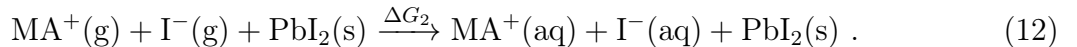
Species	E_{tot} (eV/f.u.)	$H_T - H_{0\text{K}}$ (kJ/mol)	S_T° (J mol ⁻¹ K ⁻¹)	$\tilde{\mu}_T^\circ$ (eV/f.u.)	G_T° (eV/f.u.)
MAPbI ₃ (s)	-50.93	44.79 ^a	374.13 ^a	-0.69	-51.62
PbI ₂ (s)	-8.63	19.50 ^b	174.84 ^b	-0.34	-8.97
MA ⁺ (g)	-32.84	6.20 ^b	327.7 ^b	-0.95	-33.79
I ⁻ (g)	-3.40	6.20 ^b	169.26 ^b	-0.46	-3.86
CsPbI ₃ (s)	-14.25	20.28 ^c	219.61 ^c	-0.47 ^c	-14.72
Cs ⁺ (g)	3.83	6.20 ^b	169.84 ^b	-0.46	3.37
MAI(s)	-42.36	22.25 ^d	159.7 ^d	-0.26	-5.69
CsI(s)	-5.45	13.50 ^e	123.1 ^e	-0.24	-42.62

^a Data obtained from Ref. 58; ^b Data extracted from the NIST-JANAF thermochemical tables; ^c Data extracted from Refs. 59,60; ^d Data obtained from Ref. 61; ^e Data obtained from Ref. 62.

calculate the change in Gibbs free energy ΔG_1 for the first step

$$\Delta G_1 = G_{T,\text{MA}^+(\text{g})}^\circ + G_{T,\text{I}^-(\text{g})}^\circ + G_{T,\text{PbI}_2}^\circ - G_{T,\text{MAPbI}_3}^\circ . \quad (11)$$

The calculated $\Delta G_1 = 5.0$ eV is shown in Fig. 4a. The second step of the designed cycle of MAPbI₃ dissolution in water involves the hydration of MA⁺(g) and I⁻(g)



The chemical potentials of aqueous ions $\tilde{\mu}_T^\circ(\text{aq})$ in this step can be obtained via

$$\tilde{\mu}_T^\circ(\text{aq}) = \tilde{\mu}_T^\circ + \Delta H_{\text{hyd}} - T(S_T^\circ(\text{aq}) - S_T^\circ) . \quad (13)$$

$S_T^\circ(\text{aq})$ is the entropy of an aqueous ion. Decreased enthalpies and entropies due to hydra-

tion process contribute to the values of $G_{T,MA^+(aq)}^\circ$ and $G_{T,I^-(aq)}^\circ$. Related thermodynamic properties of the second step are shown in Table 2.

Table 2: Hydration enthalpy $\Delta H_{\text{hyd}}^\circ$, entropy $S_T^\circ(\text{aq})$ of aqueous ions, and Gibbs free energy G_T° of species involved in the second step of the thermodynamic cycle of MAPbI_3 dissolution in water at room temperature 298.15 K.

Species	$\Delta H_{\text{hyd}}^\circ$ (kJ/mol)	$S_T^\circ(\text{aq})$ (J mol ⁻¹ K ⁻¹)	$\tilde{\mu}_T^\circ(\text{aq})$ (eV/f.u.)	G_T° (eV/f.u.)
$\text{MA}^+(\text{aq})$	-284.6 ^a	142.7 ^b	-3.33	-36.17
$\text{I}^-(\text{aq})$	-305.0 ^c	111.3 ^d	-3.44	-6.84
$\text{Cs}^+(\text{aq})$	-264.0 ^c	133.1 ^d	-3.08	0.75

^a Data obtained from Ref. 63; ^b Data extracted from Ref. 64; ^c Data extracted from Ref. 65; ^d Data extracted from Ref. 62.

The change of the Gibbs free energy of the second step

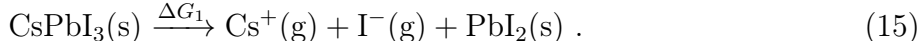
$$\Delta G_2 = G_{T,MA^+(aq)}^\circ + G_{T,I^-(aq)}^\circ - G_{T,MA^+(g)}^\circ + G_{T,I^-(g)}^\circ \quad (14)$$

amounts to $\Delta G_2 = -5.36$ eV. The strongly negative change of Gibbs free energy in the second step overcomes the Gibbs free energy gain in the first step. Combining the two-step Gibbs free energy change, we can obtain $\Delta G_{\text{diss}} = \Delta G_1 + \Delta G_2 = -0.36$ eV. The negative ΔG_{diss} of the dissolution MAPbI_3 in water at a finite concentration indicates the reaction in Eq. (7) would proceed spontaneously. The thermodynamic analysis of MAPbI_3 dissolution process suggests an intrinsic water instability of MAPbI_3 . Although the negative ΔG_{diss} reflects a spontaneity of a reaction, it only predicts the trend of the proposed reaction. According to Arrhenius equation, the rate of a reaction is controlled by the energy barrier, i.e activation energy. A low activation energy indicates a high rate constant. The low activation energy obtained from metadynamic calculations for the MAPbI_3 degradation in water demonstrates the corresponding reaction will proceed quickly. In all, for the reaction of MAPbI_3 in water, the negative ΔG_{diss} renders a thermodynamic instability and the low energy barrier points to a kinetic instability.

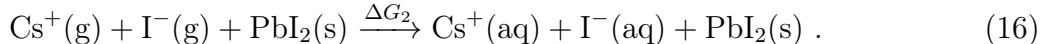
Compared with a large amount of discussions on the fragility of MAPbI_3 in water, stability

of CsPbI₃ in water recently attracts attention and is also under discussion. Lin et al.⁴⁹ indicated the water invasion triggered the phase transition of CsPbI₃ from a high-temperature cubic phase to a low-temperature orthorhombic phase and they found that water is adsorbed on the surface without penetrating the interior of CsPbI₃. Conversely, Yuan et al.⁶⁶ observed the CsPbI₃ quantum dots degraded in a chamber with a wet gas flow. They confirmed the moisture was responsible for the degradation of these CsPbI₃ quantum dots. Here, we employ the two-step thermodynamic cycle to the case of CsPbI₃ dissolution in water to clarify these controversies.

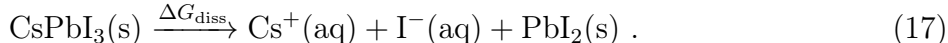
The first step of the proposed thermodynamic cycle of dissolution CsPbI₃ in water is given as



Related thermodynamic properties of species involved in the first step of CsPbI₃ dissolution in water are listed in Table 1. We can obtain the Gibbs free energy change $\Delta G_1 = 5.26$ eV for Eq. (15). The thermodynamic cycle of CsPbI₃ is shown in Fig. 4b. The second step of CsPbI₃ dissolution in water involves the hydration of Cs⁺(g) and I⁻(g)



Related thermodynamic properties are shown in Table 2. Using Gibbs free energies in Table 1 and Table 2, the change of the Gibbs free energy of the second step is estimated as $\Delta G_2 = -5.60$ eV. The overall $\Delta G_{\text{diss}} = \Delta G_1 + \Delta G_2 = -0.34$ eV for the dissolution CsPbI₃ in water



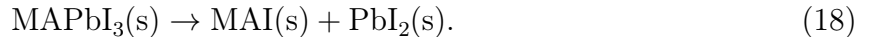
The above discussion indicates that the orthorhombic CsPbI₃ is also prone to decompose in water. The thermodynamic analysis of CsPbI₃ dissolution in water corroborates the degradation of CsPbI₃ quantum dots observed by Yuan et al.⁶⁶. The energy barrier of the



Figure 5: Thermodynamic quantities for decomposition of MAPbI₃ and CsPbI₃ via two alternative routes: a phase separation [Eq. (18)] or a dissolution in water [Eq. (7)]. ΔE_{tot} is the bare-DFT energy difference between products and the reactant (perovskite). The errorbars indicate a chemical uncertainty of the DFT exchange-correlation functional (see text for details). ΔH is the enthalpy change at $T = 298.15$ K. $T\Delta S$ captures the entropy change during decomposition. ΔG is the resultant Gibbs free energy change of MAPbI₃ and CsPbI₃ phase separation and dissolution in water.

dissolution process determines the rate of the reaction. Compared with the very low energy barrier (about 0.18 eV) for the initial dissolution of MAPbI₃, the relatively high energy barrier (greater than 0.5 eV⁴⁹) for releasing I⁻ into water from CsPbI₃ surface suggests a slow process of dissolution of CsPbI₃ which explains the differences in degradation rates at heterogeneous interfaces: water/MAPbI₃ *vs* water/CsPbI₃ observed by Lin et al.⁴⁹.

Zhang et al.⁶⁷ first used the energy differences obtained from DFT calculation to characterize the intrinsic instability of MAPbI₃ and CsPbI₃, considering a decomposition reaction of MAPbI₃ into solid state products



In Fig. 5 we show our calculated ΔE_{tot} for MAPbI₃ and CsPbI₃ which match well with ΔE_{tot} from Zhang et al.⁶⁷. According to Zhang et al.⁶⁷, a positive value of ΔE_{tot} corresponds to a stable perovskite structure. They proposed the entropy term of MAI is higher than that of MAPbI₃ which will further destabilize MAPbI₃. However, from the measurements of entropies of MAI and MAPbI₃ listed in Table 1, it clearly indicates a reverse trend. To note

that, the entropy contribution of PbI_2 cannot be neglected. The overall entropy in reaction (18) decreases and stabilizes MAPbI_3 which has been indicated in Ref. 56. The entropy gains during CsPbI_3 phase separation which is contrary to MAPbI_3 . The enthalpy change of CsPbI_3 phase separation is large enough to overcome this entropy gain resulting in a positive ΔG that is slightly greater than the value of MAPbI_3 .

The positive ΔG values for phase separation process in Fig. 5 indicate a feasibility of synthesis of MAPbI_3 and CsPbI_3 compounds. However, the result should be taken with caution, since the uncertainty in reaction energies obtained with Perdew, Burke, and Ernzerhof (PBE)²⁷ exchange-correlation functional is of the order of ± 0.03 eV/atom.⁶⁸ With five atoms per perovskite formula unit (MA^+ is considered as one cation), the estimated error is about ± 0.15 eV as shown by the errorbars in Fig. 5. When considering a water environment, the Gibbs free energy change of the decomposition reaction mentioned above decreased by 0.39 eV and becomes strongly negative. This decrease is due to hydration of MA^+/Cs^+ and Γ^- ions. The amount of enthalpy change during the designed two-step thermodynamic cycle for MAPbI_3 dissolution in water corresponding to Eq. (7) is negative (see ΔH in Fig. 5). This ΔH indicates the released energy during hydration process of MA^+ and Γ^- in Eq. (12) overcomes the energy consumed in Eq. (9). It renders the dissolution MAPbI_3 in water is an exothermic reaction. The entropy gain during the dissolution of MAPbI_3 in water further lowers ΔG in Fig. 5, suggesting the dissolution process is thermodynamically preferable. Dissimilarly, a positive $\Delta H = 0.28$ eV for CsPbI_3 dissolving in water indicates the released energy during hydration process of Cs^+ and Γ^- in Eq. (16) is less than the energy consumed during Eq. (15). This positive ΔH renders dissolution CsPbI_3 in water belongs to an endothermic reaction. Interestingly, a large entropy enhancement of dissolution CsPbI_3 in water brings down ΔG to a negative value, see in Fig. 5. This large entropy enhancement comes from the difference of a low entropy of orthorhombic CsPbI_3 and a high entropy of $\text{Cs}^+(\text{aq})$. The relative high entropy of MAPbI_3 and low entropy of CsPbI_3 in Table. 1 are consistent with the strong anharmonicity of MAPbI_3 and weak anharmonicity of CsPbI_3

recently discussed in Ref. 69,70. Compared with CsPbI₃, the large hydration enthalpy of MA⁺ ion and the entropy gain together direct the negative ΔG_{diss} . In all, we can conclude that the large hydration enthalpies of MA⁺/Cs⁺ and I⁻ and entropy enhancement as well as the low lattice energies of halide perovskite structures are responsible for the degradation of MAPbI₃/CsPbI₃ in water.

So far, we did not discuss an ionic activity a_{\pm} of CH₃NH₃I solution and its contribution $k_B T \ln(a_{\pm})$ to a chemical potential term of an electrolyte when estimating $\tilde{\mu}_T^{\circ}(\text{aq})$. The actual chemical potential of an electrolyte is expressed as

$$\mu_T \approx \tilde{\mu}_T^{\circ}(\text{aq}) + k_B T \ln(a_{\pm}). \quad (19)$$

The mean ionic activity a_{\pm} of CH₃NH₃I solution

$$a_{\pm} = (\gamma_{\pm} c / c^{\circ})^2 \quad (20)$$

is determined by its molar concentration c relative to the concentration in standard state $c^{\circ} = 1$ M and the mean ionic activity coefficient γ_{\pm} , which accounts for non-ideality of the solution. Thermodynamic data listed in Table 1 correspond to $c = 1$ M. Bonner⁷¹ and Belvèze et al.⁷² reported γ_{\pm} of MACl is 0.58 when $c = 1$ M. This value is taken as an estimation of γ_{\pm} for MAI. The additional term $k_B T \ln(a_{\pm})$ for MAI solution is estimated as -0.028 eV at $c = c^{\circ}$, which is relatively small considering $\Delta G_{\text{diss}} = -0.36$ eV. In a dilute solution limit ($c \ll 1$ M), the term $k_B T \ln(a_{\pm})$ becomes negative and drives the water decomposition reaction of MAPbI₃.⁵⁶ When decomposition proceeds to reach a finite concentration (*e.g.*, $c = c^{\circ}$), the ΔG_{diss} is no longer governed by $k_B T \ln(a_{\pm})$ but dominant by enthalpies and entropies of aqueous ions (see ΔH and $-T\Delta S$ of dissolution process in Fig. 5). Upon further dissolution, chemical potentials of the aqueous solution increase until $\Delta G_{\text{diss}} = 0$ eV, the solution is then saturated and the dissolution process ceases.

Conclusion

The water instability of MAPbI₃ is a major problem for commercialization of perovskite photovoltaics. Explanations of the underline mechanism are under debate. Here, we use *ab initio* metadynamic method to reconstruct the free energy surface of the dissolution process of MAPbI₃ in explicit water. The predictive power of metadynamics unravels the pathway of water dissolving MAPbI₃ surface. One intermediate state and two transition states are identified during the initial dissolution process. The first transition state involves breaking of I–Pb bond and formation of an intermediate state (I–MA interactions) at the surface with a low energy barrier of 0.16 eV. The second transition state corresponds to dissociation I–MA interaction and hydration of the I[−] ion with the energy barrier of 0.22 eV. In addition, using DFT calculations augmented with experimental data, the analysis of thermodynamics of MAPbI₃ decomposition in water at a finite concentration indicates a negative Gibbs free energy change which suggests the spontaneity of water dissolution of MAPbI₃. It is worthy to mention that a large hydration enthalpy of MA⁺ and a entropy gain under aqueous condition direct the negative ΔG_{diss} . Combined with the low energy barrier for ease of ions escaping from the MAPbI₃ surface and spontaneous nature of dissolving in water, it can be explained why the water immediately destroys pristine MAPbI₃. We also analyze how CsPbI₃ react with water from the thermodynamic point of view. It is found the Gibbs free energy change of dissolution CsPbI₃ in water is also a negative value similar as the value of MAPbI₃, which is consistent with an experimental observation of CsPbI₃ degradation in a moist environment. Compared with MAPbI₃, a large entropy enhancement of Cs⁺ dominates the negative ΔG_{diss} for CsPbI₃ dissolution in water. Our explanation provides a deeper insight of the water instability of MAPbI₃ and presents a perspective on improving the instability of perovskite photovoltaics in future.

Supporting Information Available

The following files are available free of charge.

The following files are available free of charge.

- Initial FES of MA⁺: The initial basin of free energy surface for MA⁺ dissolution in water is plotted and compared with the initial basin of I⁻ dissolution in water.

Acknowledgement

Authors are indebted to Prof. Claudine Katan, Dr. Mikaël Kepenekian and Prof. Xavier Rocquefelte from Université de Rennes 1 for advises on setting up the initial perovskite-water interface. The authors also thank Natural Sciences and Engineering Research Council of Canada under the Discovery Grant Programs RGPIN-2015-04518. All the calculations were performed using a Compute Canada infrastructure supported by the Canada Foundation for Innovation under the John R. Evans Leaders Fund program.

References

- (1) Kojima, A.; Teshima, K.; Shirai, Y.; Miyasaka, T. Organometal Halide Perovskites as Visible-Light Sensitizers for Photovoltaic Cells. *J. Am. Chem. Soc.* **2009**, *131*, 6050–6051.
- (2) Hailegnaw, B.; Kirmayer, S.; Edri, E.; Hodes, G.; Cahen, D. Rain on Methylammonium Lead Iodide Based Perovskites: Possible Environmental Effects of Perovskite Solar Cells. *J. Phys. Chem. Lett.* **2015**, *6*, 1543–1547.
- (3) Li, Y.; Xu, X.; Wang, C.; Wang, C.; Xie, F.; Yang, J.; Gao, Y. Degradation by Exposure of Coevaporated CH₃NH₃PbI₃ Thin Films. *J. Phys. Chem. C* **2015**, *119*, 23996–24002.

- (4) Ke, J. C.-R.; Walton, A. S.; Lewis, D. J.; Tedstone, A.; O'Brien, P.; Thomas, A. G.; Flavell, W. R. *In situ* Investigation of Degradation at Organometal Halide Perovskite Surfaces by X-ray Photoelectron Spectroscopy at Realistic Water Vapour Pressure. *Chem. Commun.* **2017**, *53*, 5231–5234.
- (5) Kakekhani, A.; Katti, R. N.; Rappe, A. M. Water in Hybrid Perovskites: Bulk MAPbI₃ Degradation *via* Super-Hydrous State. *APL Mater.* **2019**, *7*, 041112.
- (6) Philippe, B.; Park, B.-W.; Lindblad, R.; Oscarsson, J.; Ahmadi, S.; Johansson, E. M.; Rensmo, H. Chemical and Electronic Structure Characterization of Lead Halide Perovskites and Stability Behavior under Different Exposures A Photoelectron Spectroscopy Investigation. *Chem. Mater.* **2015**, *27*, 1720–1731.
- (7) Niu, G.; Li, W.; Meng, F.; Wang, L.; Dong, H.; Qiu, Y. Study on the Stability of CH₃NH₃PbI₃ Films and the Effect of Post-Modification by Aluminum Oxide in All-Solid-State Hybrid Solar Cells. *J. Mater. Chem. A* **2014**, *2*, 705–710.
- (8) Frost, J. M.; Butler, K. T.; Brivio, F.; Hendon, C. H.; Van Schilfgaarde, M.; Walsh, A. Atomistic Origins of High-Performance in Hybrid Halide Perovskite Solar Cells. *Nano Lett.* **2014**, *14*, 2584–2590.
- (9) Wei, W.; Hu, Y. H. Catalytic Role of H₂O in Degradation of Inorganic-Organic Perovskite (CH₃NH₃PbI₃) in Air. *Int. J. Energy Res.* **2016**, *41*, 1063–1069.
- (10) McLeod, J. A.; Liu, L. Prospects for Mitigating Intrinsic Organic Decomposition in Methylammonium Lead Triiodide Perovskite. *J. Phys. Chem. Lett.* **2018**, *9*, 2411–2417.
- (11) Yang, J.; Yuan, Z.; Liu, X.; Braun, S.; Li, Y.; Tang, J.; Gao, F.; Duan, C.; Fahlman, M.; Bao, Q. Oxygen- and Water-Induced Energetics Degradation in Organometal Halide Perovskites. *ACS Appl. Mater. Interfaces* **2018**, *10*, 16225–16230.

- (12) Kosasih, F. U.; Ducati, C. Characterising Degradation of Perovskite Solar Cells Through In-Situ and Operando Electron Microscopy. *Nano Energy* **2018**, *47*, 243–256.
- (13) Aristidou, N.; Eames, C.; Islam, M. S.; Haque, S. A. Insights into the Increased Degradation Rate of $\text{CH}_3\text{NH}_3\text{PbI}_3$ Solar Cells in Combined Water and O_2 Environments. *J. Mater. Chem. A* **2017**, *5*, 25469–25475.
- (14) Smecca, E.; Numata, Y.; Deretzis, I.; Pellegrino, G.; Boninelli, S.; Miyasaka, T.; Magna, A. L.; Alberti, A. Stability of Solution-Processed MAPbI_3 and FAPbI_3 Layers. *Phys. Chem. Chem. Phys.* **2016**, *18*, 13413–13422.
- (15) Saidaminov, M. I.; Kim, J.; Jain, A.; Quintero-Bermudez, R.; Tan, H.; Long, G.; Tan, F.; Johnston, A.; Zhao, Y.; Voznyy, O. et al. Suppression of Atomic Vacancies via Incorporation of Isovalent Small Ions to Increase the Stability of Halide Perovskite Solar Cells in Ambient Air. *Nat. Energy* **2018**, *3*, 648–654.
- (16) Lin, C.-C.; Lyu, Y.; Hunston, D. L.; Kim, J. H.; Wan, K.-T.; Stanley, D. L.; Gu, X. Cracking and Delamination Behaviors of Photovoltaic Backsheet after Accelerated Laboratory Weathering. Reliability of Photovoltaic Cells, Modules, Components, and Systems VIII. 2015; p 956304.
- (17) Mosconi, E.; Azpiroz, J. M.; De Angelis, F. *Ab Initio* Molecular Dynamics Simulations of Methylammonium Lead Iodide Perovskite Degradation by Water. *Chem. Mater.* **2015**, *27*, 4885–4892.
- (18) Caddeo, C.; Marongiu, D.; Meloni, S.; Filippetti, A.; Quochi, F.; Saba, M.; Mattoni, A. Hydrophilicity and Water Contact Angle on Methylammonium Lead Iodide. *Adv. Mater. Interfaces* **2018**, 1801173.
- (19) Caddeo, C.; Saba, M. I.; Meloni, S.; Filippetti, A.; Mattoni, A. Collective Molecular Mechanisms in the $\text{CH}_3\text{NH}_3\text{PbI}_3$ Dissolution by Liquid Water. *ACS nano* **2017**, *11*, 9183–9190.

- (20) Park, S.; Chang, W. J.; Lee, C. W.; Park, S.; Ahn, H.-Y.; Nam, K. T. Photocatalytic Hydrogen Generation from Hydriodic Acid Using Methylammonium Lead Iodide in Dynamic Equilibrium with Aqueous Solution. *Nat. Energy* **2017**, *2*, 16185.
- (21) Liu, L.-M.; Laio, A.; Michaelides, A. Initial Stages of Salt Crystal Dissolution Determined with *Ab Initio* Molecular Dynamics. *Phys. Chem. Chem. Phys.* **2011**, *13*, 13162–13166.
- (22) Chen, J.-C.; Reischl, B.; Spijker, P.; Holmberg, N.; Laasonen, K.; Foster, A. S. *Ab Initio* Kinetic Monte Carlo Simulations of Dissolution at the NaCl-Water Interface. *Phys. Chem. Chem. Phys.* **2014**, *16*, 22545–22554.
- (23) Laio, A.; Parrinello, M. Escaping Free-Energy Minima. *Proc. Natl. Acad. Sci. U.S.A.* **2002**, *99*, 12562–12566.
- (24) Iannuzzi, M.; Laio, A.; Parrinello, M. Efficient Exploration of Reactive Potential Energy Surfaces Using Car-Parrinello Molecular Dynamics. *Phys. Rev. Lett.* **2003**, *90*, 238302.
- (25) Bucko, T. *Ab Initio* Calculations of Free-Energy Reaction Barriers. *J. Phys.: Condens. Matter* **2008**, *20*, 064211.
- (26) Kohn, W.; Sham, L. J. Self-Consistent Equations Including Exchange and Correlation Effects. *Phys. Rev.* **1965**, *140*, A1133.
- (27) Perdew, J. P.; Burke, K.; Ernzerhof, M. Generalized Gradient Approximation Made Simple. *Phys. Rev. Lett.* **1996**, *77*, 3865.
- (28) Wang, Y.; Gould, T.; Dobson, J. F.; Zhang, H.; Yang, H.; Yao, X.; Zhao, H. Density Functional Theory Analysis of Structural and Electronic Properties of Orthorhombic Perovskite $\text{CH}_3\text{NH}_3\text{PbI}_3$. *Phys. Chem. Chem. Phys.* **2013**, *16*, 1424–1429.
- (29) Zheng, C.; Rubel, O. Aziridinium Lead Iodide: A Stable, Low-Band-Gap Hybrid Halide Perovskite for Photovoltaics. *J. Phys. Chem. Lett.* **2018**, *9*, 874–880.

- (30) Li, Y.; Yang, K. High-Throughput Computational Design of Organic-Inorganic Hybrid Halide Semiconductors beyond Perovskites for Optoelectronics. *Energy Environ. Sci.* **2019**, *12*, 2233–2243.
- (31) Klimeš, J.; Bowler, D. R.; Michaelides, A. Chemical Accuracy for the Van Der Waals Density Functional. *J Phys. Condens. Matter* **2009**, *22*, 022201.
- (32) Grimme, S.; Antony, J.; Ehrlich, S.; Krieg, H. A Consistent and Accurate *Ab Initio* Parametrization of Density Functional Dispersion Correction (DFT-D) for the 94 Elements H-Pu. *J. Chem. Phys.* **2010**, *132*, 154104.
- (33) Kresse, G.; Furthmüller, J. Efficient Iterative Schemes for *Ab Initio* Total-Energy Calculations Using A Plane-Wave Basis Set. *Phys. Rev. B* **1996**, *54*, 11169.
- (34) Kresse, G.; Joubert, D. From Ultrasoft Pseudopotentials to the Projector Augmented-Wave Method. *Phys. Rev. B* **1999**, *59*, 1758.
- (35) Blöchl, P. Projector Augmented-Wave Method. *Phys. Rev. B* **1994**, *50*, 17953.
- (36) Zheng, C.; Rubel, O. Ionization Energy as a Stability Criterion for Halide Perovskites. *J. Phys. Chem. C* **2017**, *121*, 11977–11984.
- (37) Monkhorst, H. J.; Pack, J. D. Special Points for Brillouin-Zone Integrations. *Phys. Rev. B* **1976**, *13*, 5188–5192.
- (38) Zheng, C.; Yu, S.; Rubel, O. Structural Dynamics in Hybrid Halide Perovskites: Bulk Rashba Splitting, Spin Texture, and Carrier Localization. *Phys. Rev. Materials* **2018**, *2*, 114604.
- (39) Whitfield, P.; Herron, N.; Guise, W.; Page, K.; Cheng, Y.; Milas, I.; Crawford, M. Structures, Phase Transitions and Tricritical Behavior of the Hybrid Perovskite Methyl Ammonium Lead Iodide. *Sci. Rep.* **2016**, *6*, 35685.

- (40) She, L.; Liu, M.; Zhong, D. Atomic Structures of $\text{CH}_3\text{NH}_3\text{PbI}_3$ (001) Surfaces. *ACS Nano* **2015**, *10*, 1126–1131.
- (41) Ohmann, R.; Ono, L. K.; Kim, H.-S.; Lin, H.; Lee, M. V.; Li, Y.; Park, N.-G.; Qi, Y. Real-Space Imaging of the Atomic Structure of Organic–Inorganic Perovskite. *J. Am. Chem. Soc.* **2015**, *137*, 16049–16054.
- (42) Nosé, S. A Unified Formulation of the Constant Temperature Molecular Dynamics Methods. *J. Chem. Phys.* **1984**, *81*, 511–519.
- (43) Hoover, W. G. Canonical Dynamics: Equilibrium Phase-Space Distributions. *Phys. Rev. A* **1985**, *31*, 1695.
- (44) Ensing, B.; Laio, A.; Parrinello, M.; Klein, M. L. A Recipe for the Computation of the Free Energy Barrier and the Lowest Free Energy Path of Concerted Reactions. *J. Phys. Chem. B* **2005**, *109*, 6676–6687.
- (45) Karmakar, A.; Chandra, A. Water in Hydration Shell of An Iodide Ion: Structure and Dynamics of Solute-Water Hydrogen Bonds and Vibrational Spectral Diffusion from First-Principles Simulations. *J. Phys. Chem. C* **2015**, *119*, 8561–8572.
- (46) Bonomi, M.; Branduardi, D.; Bussi, G.; Camilloni, C.; Provasi, D.; Raiteri, P.; Donadio, D.; Marinelli, F.; Pietrucci, F.; Broglia, R. A. PLUMED: A Portable Plugin for Free-Energy Calculations with Molecular Dynamics. *Comput. Phys. Commun.* **2009**, *180*, 1961–1972.
- (47) Momma, K.; Izumi, F. VESTA 3 for Three-Dimensional Visualization of Crystal, Volumetric and Morphology Data. *J. Appl. Crystallogr.* **2011**, *44*, 1272–1276.
- (48) Markovich, G.; Giniger, R.; Levin, M.; Cheshnovsky, O. Photoelectron Spectroscopy of Iodine Anion Solvated in Water Clusters. *J. Chem. Phys.* **1991**, *95*, 9416–9419.

- (49) Lin, J.; Lai, M.; Dou, L.; Kley, C. S.; Chen, H.; Peng, F.; Sun, J.; Lu, D.; Hawks, S. A.; Xie, C. Thermochromic Halide Perovskite Solar Cells. *Nat. Mater.* **2018**, *17*, 261–267.
- (50) Ohtaki, H.; Fukushima, N.; Hayakawa, E.; Okada, I. Dissolution Process of Sodium Chloride Crystal in Water. *Pure Appl. Chem.* **1988**, *60*, 1321–1324.
- (51) Yang, Y.; Meng, S.; Xu, L. F.; Wang, E. G.; Gao, S. Dissolution Dynamics of NaCl Nanocrystal in Liquid Water. *Phys. Rev. E* **2005**, *72*, 012602.
- (52) Fedotova, M.; Kruchinin, S. Hydration of Methylamine and Methylammonium Ion: Structural and Thermodynamic Properties from the Data of the Integral Equation Method in the RISM Approximation. *Russ. Chem. Bull.* **2012**, *61*, 240–247.
- (53) Delugas, P.; Filippetti, A.; Mattoni, A. Methylammonium Fragmentation in Amines as Source of Localized Trap Levels and the Healing Role of Cl in Hybrid Lead-Iodide Perovskites. *Phys. Rev. B* **2015**, *92*, 045301.
- (54) Fan, Z.; Xiao, H.; Wang, Y.; Zhao, Z.; Lin, Z.; Cheng, H.-C.; Lee, S.-J.; Wang, G.; Feng, Z.; Goddard III, W. A. Layer-by-Layer Degradation of Methylammonium Lead Tri-iodide Perovskite Microplates. *Joule* **2017**, *1*, 548–562.
- (55) Sholl, D.; Steckel, J. A. *Density Functional Theory: a Practical Introduction*; John Wiley & Sons: Hoboken, New Jersey, 2011.
- (56) Tenuta, E.; Zheng, C.; Rubel, O. Thermodynamic Origin of Instability in Hybrid Halide Perovskites. *Sci. Rep.* **2016**, *6*, 37654.
- (57) Kye, Y.-H.; Yu, C.-J.; Jong, U.-G.; Ri, K.-C.; Kim, J.-S.; Choe, S.-H.; Hong, S.-N.; Li, S.; Wilson, J. N.; Walsh, A. Vacancy-Driven Stabilization of the Cubic Perovskite Polymorph of CsPbI₃. *J. Phys. Chem. C* **2019**, *123*, 9735–9744.
- (58) Onoda-Yamamuro, N.; Matsuo, T.; Suga, H. Calorimetric and IR Spectroscopic Studies

- of Phase Transitions in Methylammonium Trihalogenoplumbates (II). *J. Phys. Chem. Solids* **1990**, *51*, 1383–1395.
- (59) Ong, S. P.; Cholia, S.; Jain, A.; Brafman, M.; Gunter, D.; Ceder, G.; Persson, K. A. The Materials Application Programming Interface (API): a Simple, Flexible and Efficient API for Materials Data Based on REpresentational State Transfer (REST) Principles. *Comput. Mater. Sci.* **2015**, *97*, 209–215.
- (60) Hinuma, Y.; Pizzi, G.; Kumagai, Y.; Oba, F.; Tanaka, I. Band Structure Diagram Paths Based on Crystallography. *Comput. Mater. Sci.* **2017**, *128*, 140–184.
- (61) Yamamuro, O.; Oguni, M.; Matsuo, T.; Suga, H. Calorimetric and Dilatometric Studies on the Phase Transitions of Crystalline $\text{CH}_3\text{NH}_3\text{I}$. *J. Chem. Thermodyn.* **1986**, *18*, 939–954.
- (62) Rumble, J. *CRC Handbook of Chemistry and Physics*; CRC press: Boca Raton, Florida, 2017.
- (63) Housecroft, C. E.; Jenkins, H. D. B. Absolute Ion Hydration Enthalpies and the Role of Volume within Hydration Thermodynamics. *RSC Adv.* **2017**, *7*, 27881–27894.
- (64) Marcus, Y.; Loewenschuss, A. Chapter 4. Standard Entropies of Hydration of Ions. *Annu. Rep. Prog. Chem., Sect. C: Phys. Chem.* **1984**, *81*, 81–135.
- (65) Smith, D. W. Ionic Hydration Enthalpies. *J. Chem. Educ.* **1977**, *54*, 540–542.
- (66) Yuan, G.; Ritchie, C.; Ritter, M.; Murphy, S.; Gómez, D. E.; Mulvaney, P. The Degradation and Blinking of Single CsPbI_3 Perovskite Quantum Dots. *J. Phys. Chem. C* **2017**, *122*, 13407–13415.
- (67) Zhang, Y.; Chen, S.; Xu, P.; Xiang, H.; Gong, X.; Walsh, A.; Wei, S. Intrinsic Instability of the Hybrid Halide Perovskite Semiconductor $\text{CH}_3\text{NH}_3\text{PbI}_3$. *Chin. Phys. Lett.* **2018**, *35*, 036104.

- (68) Hautier, G.; Ong, S. P.; Jain, A.; Moore, C. J.; Ceder, G. Accuracy of Density Functional Theory in Predicting Formation Energies of Ternary Oxides from Binary Oxides and Its Implication on Phase Stability. *Phys. Rev. B* **2012**, *85*, 155208.
- (69) Zhu, T.; Ertekin, E. Mixed Phononic and Non-Phononic Transport in Hybrid Lead Halide Perovskites: Glass-Crystal Duality, Dynamical Disorder, and Anharmonicity. *Energy Environ. Sci.* **2019**, *12*, 216–229.
- (70) Marronnier, A.; Roma, G.; Boyer-Richard, S.; Pedesseau, L.; Jancu, J.-M.; Bonnassieux, Y.; Katan, C.; Stoumpos, C. C.; Kanatzidis, M. G.; Even, J. Anharmonicity and Disorder in the Black Phases of Cesium Lead Iodide Used for Stable Inorganic Perovskite Solar Cells. *ACS nano* **2018**, *12*, 3477–3486.
- (71) Bonner, O. D. Osmotic and Activity Coefficients of Methyl-Substituted Ammonium Chlorides. *J. Chem. Soc. Faraday Trans.* **1981**, *77*, 2515–2518.
- (72) Belvèze, L. S.; Brennecke, J. F.; Stadtherr, M. A. Modeling of Activity Coefficients of Aqueous Solutions of Quaternary Ammonium Salts with the Electrolyte-NRTL Equation. *Ind. Eng. Chem. Res* **2004**, *43*, 815–825.

Graphical TOC Entry

